High-order-harmonic generation driven by pulses with angular spatial chirp

Carlos Hernández-García,[1,2,*] Agnieszka Jaron-Becker,[1,3] Daniel D. Hickstein,[1] Andreas Becker,[1,3] and Charles G. Durfee[1,4]

[1]*JILA, University of Colorado and NIST, Boulder, Colorado 80309-0440, USA*
[2]*Grupo de Investigación en Aplicaciones del Láser y Fotónica, University of Salamanca, E-37008, Salamanca, Spain*
[3]*Department of Physics, University of Colorado, Boulder, Colorado 80309-0440, USA*
[4]*Department of Physics, Colorado School of Mines, Golden, Colorado 80401, USA*

We present and analyze a technique to drive high-order harmonics by laser pulses with an angular spatial chirp. Results of our numerical simulations show that each harmonic is emitted with an angular chirp which scales inversely with the harmonic order and leads to additional control of the spatial and temporal resolution of the spectrum. In particular, the use of angular chirp leads to separation of the harmonics in two dimensions where (i) high spectral resolution can be achieved and (ii) the temporal periodicity of the harmonic pulse trains can be controlled. We show that this technique does not require carrier-envelope-phase stabilization when using few-cycle laser pulses.

I. INTRODUCTION

High-order-harmonic generation (HHG) and attosecond science continue to be rapidly evolving areas of research and application [1–7]. The highly nonlinear mechanism responsible for the generation of high-order harmonics is simply understood in semiclassical terms [8,9]: An electron is tunnel ionized from an atom or molecule by an intense linearly polarized laser field, then accelerated, and finally driven back to its parent ion, releasing the kinetic energy acquired from the field in the form of high-order-harmonic radiation upon recollision, extending from the extreme ultraviolet to the soft x-ray regime [10]. This radiation is emitted in the form of attosecond pulses [11–13], potentially with modulations leading to wave forms on the zeptosecond time scale [14]. These two remarkable characteristics of the high-order harmonics (high energy in the form of ultrashort pulses) have made them unique tools with a broad range of applications [7,15].

Over the last two decades many efforts have been made to control the temporal and spectral characteristics of the high-order harmonics, most of them relying in the fact that the properties of the driving field are imprinted in the harmonic beam. For example, it has been recently demonstrated that orbital and spin angular momentum are conserved during the HHG process [16,17]. Another interesting recent development in HHG has been the use of spatially chirped pulses to drive harmonics in the extreme-ultraviolet regime. In the so-called lighthouse effect [18], the pump beam is focused so that at the beam waist there is a transverse spatial chirp, where the local central frequency varies smoothly across the beam profile [see Fig. 1(a)]. This variation of the local frequency across the focal spot leads to wave fronts with surface normal directions that vary from one cycle to the next. Therefore, in successive recollision processes the high-energy photons are emitted in different directions, allowing the attosecond pulses to be separated in the far field [19,20]. In this work, we will analyze the effect of driving harmonics by a beam with angular spatial chirp, which is complementary to transverse

spatial chirp in the following sense. Note that in the lighthouse effect, the transverse spatial chirp at the focus is generated by introducing angular spatial chirp before the focusing element. In our proposed techniques, transverse spatial chirp at the lens entrance is used to give angular spatial chirp at the focus. This configuration is known as simultaneous space-time focusing (SSTF) [21]: The on-axis intensity is strongly localized because the pulse duration is not its shortest until all frequency components are fully overlapped [22] [see Fig. 1(d)]. SSTF has previously been applied to nonlinear microscopy, micromachining, and laser surgery [23–25].

One of the consequences of angular spatial chirp is a strong pulse front tilt [see Fig. 1(f)]. When applied to HHG, the high-order harmonics are driven by wave fronts that are parallel, but with successive transverse offset. The analysis we present here shows that this results in a spectrum of each harmonic that is angularly dispersed with a chirp rate that can be predicted with a simple scaling rule. When a grating is used to separate the harmonic orders, the harmonic spectrum is therefore spread over two dimensions, yielding a type of hyperspectral combination of coarse and fine spectral resolution. In the time domain, the far-field attosecond pulse train is seen to have a periodicity that varies with observation angle. As a consequence, both the spectral resolution as well as the temporal periodicity can be controlled by adjusting the angular chirp imprinted to the fundamental beam. If driven by few-cycle laser pulses, the angular distribution of the HHG spectrum is not sensitive to carrier-envelope phase (CEP) variations. This technique could therefore lead to improvements in the spectral and temporal resolution in ultrafast absorption experiments [26,27].

The paper is organized as follows. First, in Sec. II we present a brief analysis of SSTF, in particular analyzing the differences between pure transverse chirp and pure angular chirp at focus. Then, in Sec. III we present our theoretical results of HHG driven by angularly chirped laser pulses. We show how this technique improves the spectral resolution of the harmonic source for multicycle and few-cycle driving pulses. In the latter case, we present the angular distribution of the attosecond pulse trains emitted. Finally, we demonstrate that this technique is still valid even when there are variations in

*carloshergar@usal.es
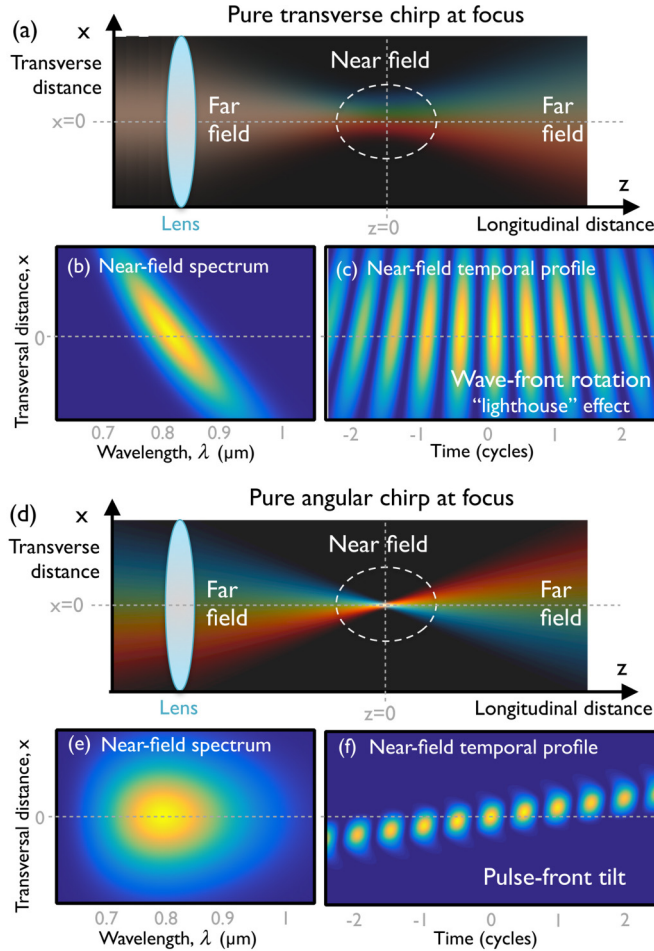
FIG. 1. (a) Schematic of a beam with transverse chirp at the focal plane, with the transverse spectrum, $|E(x,\lambda)|^2$ (b) and temporal profile, $\mathrm{Re}[E(x,t)]^2$ (c) of the electric field E at the focal plane. The variation of the local frequency across the focal spot leads to wave fronts with surface normal directions that vary from one cycle to the next, which has been applied to obtain the so-called lighthouse effect. (d) Schematic of a beam with angular chirp at the focal plane proposed in this work to drive HHG: A transverse spatially chirped beam is focused, so each frequency beam propagates along a different direction, overlapping at the focal plane. The transverse spectrum $|E(x,\lambda)|^2$ (e) and temporal profile $\mathrm{Re}[E(x,t)]^2$ (f) of the electric field E are shown both at the focal plane, where the beam exhibits a pulse front tilt with wave fronts all perpendicular to the optical axis.

the CEP of the driving laser. The paper ends with a brief summary.

II. SIMULTANEOUS SPATIAL AND TEMPORAL FOCUSING

In spatially chirped beam propagation each frequency component has an angle and/or transverse position that depends on the frequency difference from the central frequency ω_0. As discussed in the introduction, there are two limiting cases, where the spatial chirp is either purely angular [Fig. 1(d)] or transverse [Fig. 1(a)]. Let us start by analyzing the case of pure transverse spatial chirp, where all the spectral components travel as beamlets in the same direction but with a transverse

offset proportional to the frequency offset: $x_s(\omega) = \alpha(\omega - \omega_0)$ (α is the transverse chirp rate). The field in the frequency domain in the transverse (x,y) plane for this configuration is given by

$$
E(x,y,\omega) = E_0 \exp\left[-\frac{(\omega - \omega_0)^2}{\Delta\omega^2}\right]
$$
$$
\times \exp\left[-\frac{[x - x_s(\omega)]^2 + y^2}{w^2}\right], \qquad (1)
$$

where $\Delta\omega$ is the spectral bandwidth. For simplicity, we assume zero overall spectral phase [$\phi(\omega) = 0$] and that each beamlet is collimated with spot radius w. Two optical systems for producing such a beam are an angularly dispersing element at the back focal plane of a lens [21,28] or a single pass through a pair of parallel gratings [23]. Since the local central frequency varies spatially [Fig. 1(b)], the wave-front directions rotate in time [Fig. 1(c)]. The attosecond lighthouse effect in HHG can be realized when a beam is produced with transverse spatial chirp near a focal plane such that α is optimized to maximize the wave-front rotation angles [18].

Next we consider the case of pure angular chirp [Fig. 1(d)], where all the spectral components are overlapped [Fig. 1(e)], but the beam angle θ_x changes with the frequency. Here the field can be written as

$$
E(x,y,\omega) = E_0 \exp\left[-\frac{(\omega - \omega_0)^2}{\Delta\omega^2}\right] \exp\left[-\frac{x^2 + y^2}{w^2}\right]
$$
$$
\times \exp\left[i\frac{\omega}{c}\sin\theta_x(\omega)x\right]. \qquad (2)
$$

A beam with transverse spatial chirp directed into to a lens or curved mirror will produce a beam with pure angular chirp at the focal plane [see Fig. 1(d)]. In this case, the angular chirp rate (γ_0) can be expressed by

$$
\tan\theta_x(\omega) = -\alpha(\omega - \omega_0)/f \equiv \gamma_0(\omega - \omega_0), \qquad (3)
$$

where f is the lens focal length. We will use the small angle approximation where $\tan\theta_x \approx \sin\theta_x$. This condition where the beamlet waist position coincides with the plane where the spectral components overlap with an angular sweep is the case found in SSTF [21]. Note that the two limiting cases considered here are Fourier complements of each other [Fig. 1(d)] and vice versa [Fig. 1(a)]. This property was exploited in an interferometric characterization technique to characterize spatial chirp [29].

From now on, we will concentrate on the case of a beam with pure angular chirp at focus [Fig. 1(d)]. For HHG we are primarily concerned with the phase and envelope structure of the field at the focal plane (the near field). Although the full beam at the lens entrance is elliptical, for small angular range, the resulting time-averaged focal spot is round, since each beamlet focuses to a round spot and all the spectral components overlap. At the focal plane, the spectral phase of the pulse can be written as $\phi(x,\omega) = \omega \sin\theta_x(\omega)x/c$ and hence the group delay given by [22]

$$
\tau_g(x) = \left.\frac{\partial}{\partial\omega}\phi\right|_{\omega=\omega_0} = \gamma_0\frac{\omega_0}{c}x \qquad (4)
$$

varies linearly across the focal spot [Fig. 1(f)]. This pulse front tilt is a direct consequence of the angular chirp when the frequency components are overlapped. Furthermore, the second-order spectral chirp, $\phi_2 = 2\gamma_0 x/c$, depends linearly on x as well and is significant when $\gamma_0 w_0 \Delta\omega^2/c > 1$, where w_0 is the focal spot radius and $\Delta\omega$ is the spectral bandwidth [22]. Although the pulse envelope is tilted, the cycle-to-cycle wave fronts are mutually parallel [see Fig. 1(f)] when ϕ_2 is not important. As the pulse travels to the far field, the spectral components separate spatially, resulting in some wave-front rotation.

III. ANGULARLY CHIRPED HIGH-ORDER-HARMONIC GENERATION

The effect of the pulse front tilt on HHG can be understood qualitatively as follows: At the focal plane, the spatiotemporal distribution of the driving pulse is conveyed to the nonlinear polarization that results in the harmonic emission. The harmonic source will have the same pulse front tilt but the central frequency will be $\omega_q = q\omega_0$, where q is the harmonic order. Referring to Eq. (4), we therefore expect that each harmonic will be emitted with an angular chirp rate $\gamma_q = \gamma_0/q$ that decreases with harmonic order. Thus, attosecond pulses with rotating direction in the far field and some spatial separation in the near field will be generated, which is the inverse of what is found with the lighthouse effect. In the following, we present our theoretical method for computing HHG and propagation driven by angularly chirped laser pulses. Then we present the angular distribution of the HHG spectra driven by multicycle and few-cycle laser pulses. For the latter case, we present the angular distribution of the attosecond pulse trains emitted. Finally, we analyze the robustness of this technique against variations of the carrier-envelope phase of the driving pulse.

A. Theoretical method

To model HHG, we express the fundamental field analytically using the paraxial Gaussian beam formulation [22]. Each frequency component travels as a Gaussian beam at a small tilt angle θ_x to the optical axis:

$$E(x,y,z;t) = E_0(t)A(x,y,z)\exp[i\phi(x,y,z)] \quad (5)$$

with the temporal distribution

$$E(t) = E_0 \sin^2(\pi t/2\sqrt{2}\tau_p)\cos(2\pi ct/\lambda + \phi_{CEO}), \quad (6)$$

where we used wavelength $\lambda = 800$ nm, intensity pulse duration $\tau_p = 7.7$ fs in FWHM, carrier-envelope offset $\phi_{CEO} = 0$, and peak intensity $E_0^2 = 2 \times 10^{14}$ W/cm^2 in the numerical simulations. The spatial amplitude and phase of each frequency beamlet are given by [22]

$$A(x,y,z) = \frac{w_0}{w(z)}\exp\left[-\frac{(x - z\sin\theta_x)^2 + y^2}{w^2(z)}\right] \quad (7)$$

and

$$\phi(x,y,z) = k_0 x \sin\theta_x + k_0 z\left(1 - \frac{1}{2}\sin^2\theta_x\right) - \eta(z)$$
$$+ k_0 \frac{(x - z\sin\theta_x)^2 + y^2}{2R(z)} \quad (8)$$

with beam radius $w(z) = w_0\sqrt{1 + z^2/z_R^2}$, radius of curvature $R(z) = z(1 + z_R^2/z^2)$, and Gouy phase $\eta(z) = \arctan(z/z_R)$, where $z_R = k_0 w_0^2/2$ is the Rayleigh range and $k_0 = \omega_0/c$. In the simulations we consider focusing the Gaussian beamlets with a 50-cm-focal-length lens. The beam waist at the lens is $w_{in} = 2.5$ mm, resulting in a beam waist at focus of $w_0 = 50\,\mu$m, and the angular chirp is included through the parameter γ_0.

We compute harmonic propagation by discretizing the gas jet target into elementary radiators and simulating the propagation of the emitted field $\mathbf{E}_j(\mathbf{r}_j, t)$ towards the detector as [30]

$$\mathbf{E}_j(\mathbf{r}_d, t) = \frac{q_j\mathbf{s}_d}{c^2|\mathbf{r}_d - \mathbf{r}_j|} \times \left[\mathbf{s}_d \times \mathbf{a}_j\left(t - \frac{|\mathbf{r}_d - \mathbf{r}_j|}{c}\right)\right], \quad (9)$$

where q_j is the charge of the electron, $\mathbf{s}_d$ is the unitary vector pointing to the detector, and $\mathbf{r}_d$ and $\mathbf{r}_j$ are the position vectors of the detector and of the elementary radiator j, respectively. The dipole acceleration $\mathbf{a}_j$ of each elementary source is computed using the SFA+ method [31], an extension of the strong field approximation (SFA). The signal at the detector is computed as the coherent addition of the HHG contributions of all the elementary sources where the HHG light is assumed to propagate to the detector with a phase velocity c. Propagation effects of the fundamental field, including plasma and neutral dispersion as well as time-dependent group velocity walk-off [32], are taken into account. The absorption of the harmonics in the gas is modeled using Beer's law. In our simulations the generating medium is an argon gas jet, modeled using a Gaussian function of 0.5 mm FWHM along the propagation direction, at a pressure of 5 Torr, and centered at the focus position.

B. Results in the spectral domain: Improving spectral resolution of HHG

In Fig. 2 we present the spatial far-field distribution of the high-order harmonics driven by (a) a nonchirped beam ($\gamma_0 = 0$) and by an angularly chirped beam with (b) $\gamma_0 = 16.4$ as and (c) $\gamma_0 = 35.0$ as. The vertical axis represents the photon energy, expressed in terms of harmonic order, whereas the divergence angle, in mrad, is displayed on the horizontal axis. In the nonchirped case [Fig. 2(a)], the harmonics are mainly emitted on axis, as expected. However, as we increase the angular chirp rate of the input beam, each harmonic is emitted with angular chirp as well. Note that without dispersion in the vertical direction, the harmonic orders would be overlapped. Using a grating to introduce angular dispersion in the direction normal to the plane of angular chirp results in the observed tilt of each harmonic seen in the figure. The slope for each harmonic increases linearly with the harmonic order q (dashed pink lines), which agrees well with the predicted angular chirp rate $\gamma_q = \gamma_0/q$, since the results are plotted as function of angle. However, we note a deviation from the model for the highest harmonics near the cutoff. We attribute this to the fact that the cutoff harmonics are generated during the central cycle only and, hence, do not experience the full pulse front tilt effect.

The angularly chirped high-order harmonics can be applied as a two-dimensional spectroscopic tool, as depicted in
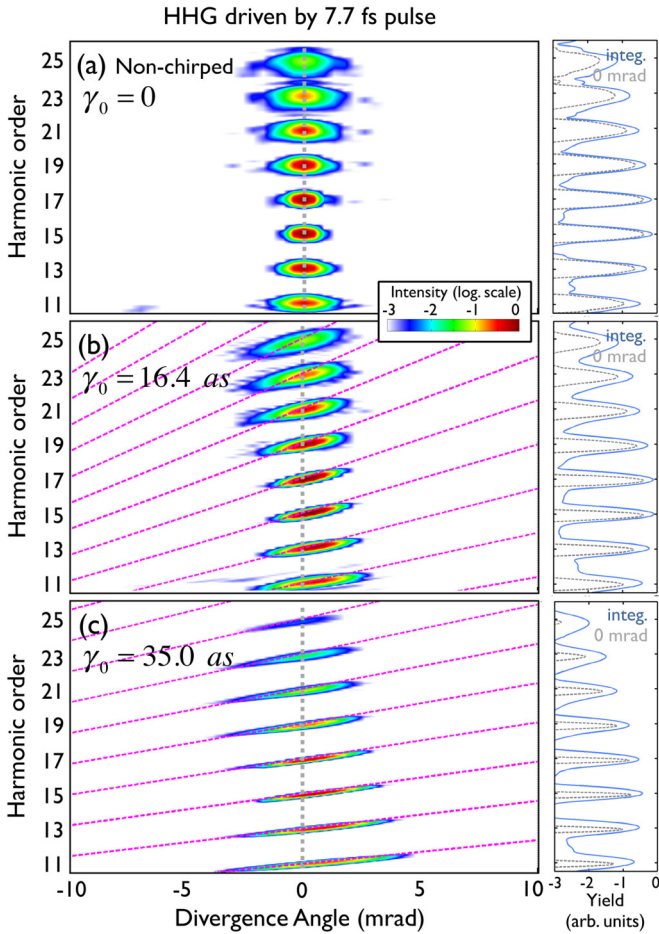
FIG. 2. Angular distribution of high-order harmonics driven by a nonchirped (a) and an angularly chirped beam with (b) $\gamma_0 = 16.4$ as and (c) $\gamma_0 = 35.0$ as (other parameters: $\lambda = 800$ nm, $\tau_p = 7.7$ fs, $\phi_{CEO} = 0$, $E_0^2 = 2 \times 10^{14}$ W/cm^2). The dashed pink line represents the fitted angular chirp rate $\gamma_q = \gamma_0/q$. On the right of each panel is shown the angularly integrated (blue line) and the on-axis (dashed gray line) spectrum.

Figs. 2(b) and 2(c). In the vertical direction, the HHG spectrum is dispersed in space as it is typically done with a grating. Additionally, in the horizontal direction, the angular chirp leads to spatial dispersion with high spectral resolution (due to the angular chirp) while maintaining a large spectral coverage (due to the wide harmonic spectrum). The separation of the harmonics in the horizontal direction provides an extra control which can be useful for spectroscopic applications.

In order to give an insight into the resolution that can be achieved in the horizontal direction, we compare in Fig. 2 (insets on the right of each panel) the incoherently integrated spectrum over the angular domain (blue line) to that emitted on axis (dashed gray line). First, note that the angularly integrated spectrum is similar for the nonchirped and chirped cases. At the atomic level, the incident pulse duration and the mechanism for generating the harmonics is identical to the case where the transform-limited pulse is focused conventionally. However, while the angle-integrated spectrum is not largely affected by the angular chirp, the increase of the angular chirp rate γ_0

leads to a narrowing of the on-axis spectra compared to the angularly integrated one.

Let us now estimate the spectral resolution in the angularly chirped direction. From Eq. (4), the spectral resolution of the qth-order harmonic, with angular dispersion γ_q, can be approximated for small divergence angles as $\Delta\omega_r \simeq \theta_x(\omega)/\gamma_q$. However, to quantitatively estimate the spectral resolution we need to consider the divergence of the individual frequency beamlets. To do so, we treat each frequency component as an individual Gaussian beamlet, with a far-field spot size of W_q. In that case, the spectral resolution at a distance z from the target can be expressed as $\Delta\omega_r = W_q/z\gamma_q$. Provided that the spectrometer camera is placed at a distance $z \gg z_{Rq} = k_q w_q^2/2$, we can approximate the far-field (W_q) and near-field (w_q) harmonic spot size relationship as $W_q \approx 2z/k_q w_q$. The spectral resolution can be written as

$$\Delta\omega_r \approx 2/k_q w_q \gamma_q \qquad (10)$$

Thus the spectral resolution of a given experiment can be increased by changing two parameters of the HHG setup. The first is by using a smaller input beamlet size, leading to a larger harmonic beamlet size (w_q) at the focus. Since HHG is highly nonperturbative, the amplitude of the harmonic field scales with a power of p, lower than q [33], being approximately constant ($p \approx 8$, according to our calculations) for the harmonics in the plateau region. Thus, the harmonic spot size is expected to scale as $w_q = w_0/\sqrt{p}$. The second is by increasing the angular chirp rate γ_0, and, hence, that of the harmonics γ_q. As a conclusion, the angular chirp can be used as a two-dimensional spectroscopic tool, allowing, for example, the simultaneous observation of multiple absorption lines in a sample spanning a wide spectral range.

Let us consider a quantitative example. In a recent experiment [26], Wang and coworkers investigated time-resolved autoionization resonances. The resonances were 80 and 23 meV in the neighborhood of 27 eV [34]. Using a transmission grating (2000 lines/mm), they obtained a spectral resolution of 50 meV. For the conditions calculated in Fig. 2(c), we obtain a fractional resolution $\Delta\omega_r/\omega_q \approx 0.8\%$, which would lead to an energy resolution of about 14 meV for $q = 21$. Certainly, higher resolution can be obtained at a particular harmonic energy by using a high-dispersion grating. But by spreading the spectrum into two dimensions, our proposed technique results in good spectral resolution and good spectral coverage simultaneously.

If shorter laser pulses are used, the harmonic bandwidth can be extended towards obtaining a continuum, as can be observed in Fig. 3(a), where we present the spatial far-field distribution of the high-order harmonics driven by a nonchirped, $\tau_p = 3.8$ fs laser pulse, with $\phi_{CEO} = 0$. Introducing angular chirp in the few-cycle driving field, and combined with grating dispersion, the harmonics remain separated rather than overlapping each other. The extra bandwidth extends each harmonic spectrum along the same slope as seen in Fig. 3(b1), where the $\tau_p = 3.8$ fs laser beam presents an angular chirp rate of $\gamma_0 = 16.4$ as. Whereas the angular spectral integration leads to the typical continuum structure obtained for HHG driven by few-cycle laser pulses [blue line on the right panel of Fig. 3(b1), and very similar to that of Fig. 3(a)], discrete harmonic peaks are obtained at
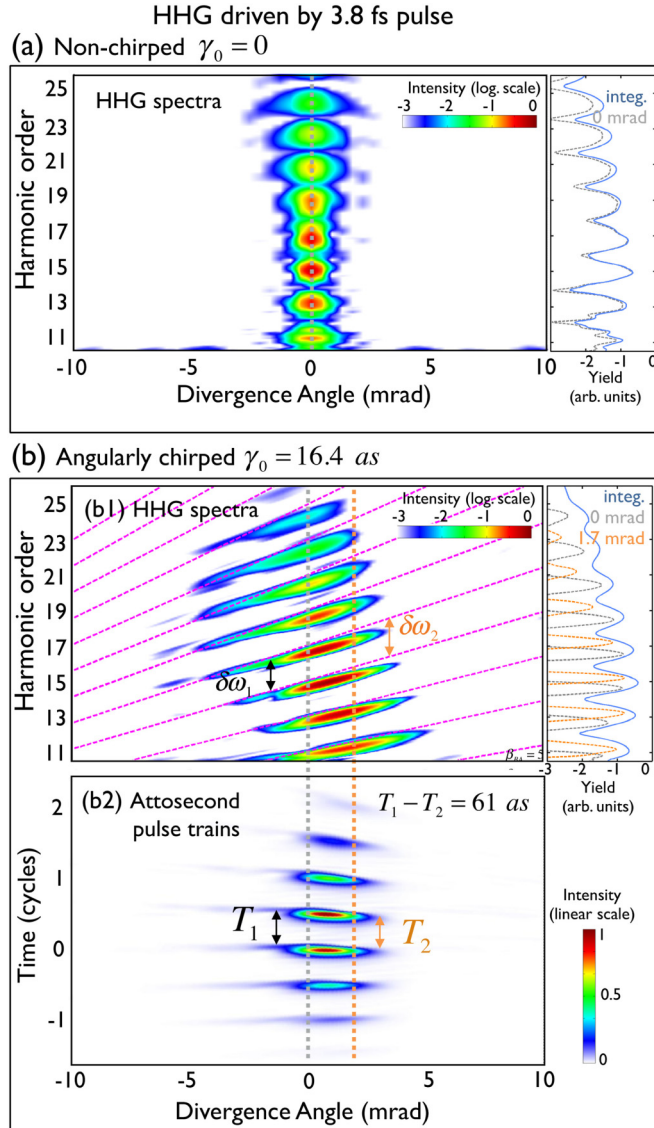
FIG. 3. Angular distribution of the high-order harmonics driven by a $\tau_p = 3.8$ fs pulse, (a) without angular chirp and (b) angularly chirped with $\gamma_0 = 16.4$ as. All other parameters of the beam are as in Fig. 2. On the right of panels (a) and (b1) are shown the angularly integrated (blue line) and the on-axis (dashed gray line) spectrum. For the angularly chirped case, an additional spectrum at 1.75 mrad is shown (orange dashed line). The dashed pink line in panel (b1) represents the model through the expected angular chirp rate $\gamma_q = \gamma_0/q$ for each odd harmonic order. In panel (b2) we present the angular distribution of the attosecond pulse trains after Fourier transform of the spectra in panel (b1) and filtering the low-order harmonics $q \leqslant 9$. Note, that the intensity yield is shown in logarithmic scale in panel (b1) but in linear scale in panel (b2). The periodicity of the attosecond pulse trains detected on axis (T_1) and at 1.75 mrad off axis (T_2) is modified by $T_2 - T_1 = 61$ as.

each angular position (two examples are shown at 0 and 1.75 mrad, indicated by the gray dashed and orange dashed lines respectively). In the target region (near field), a short burst of attosecond pulses is produced locally. But, across the focal spot, there is a train of pulses following the tilted pulse front of the fundamental [see Fig. 4(a)]. These pulses
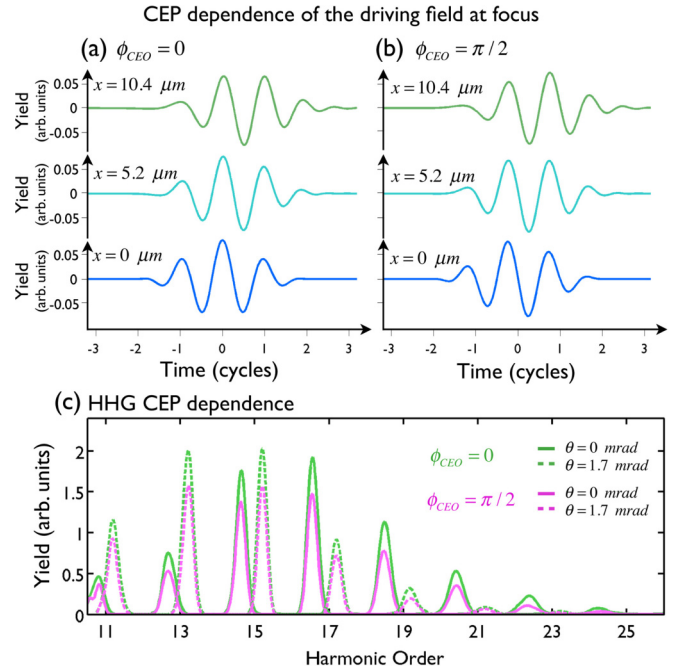
FIG. 4. CEP invariance of angularly chirped HHG. Panels (a) and (b) show the electric field at focus ($z = 0$) at three different transversal positions ($x = 0, 5.2$, and 10.4 μm), with $\phi_{CEO} = 0$ and $\phi_{CEO} = \pi/2$. (c) HHG spectrum (linear scale) detected at two angles (0 mrad, solid lines; 1.7 mrad, dashed lines), driven by an input angularly chirped beam with $\tau_p = 3.8$ fs, $\gamma_0 = 16.4$ as, and $\phi_{CEO} = 0$ (green) and $\phi_{CEO} = \pi/2$ (pink).

mix in the far field, leading to the well-defined harmonic peak structure.

C. Results in the temporal domain: Controlling the periodicity of attosecond pulses

We now analyze the temporal domain of the harmonic emission by Fourier transforming the spectra after properly filtering the low-order harmonics. In Fig. 3(b2) we present the angularly resolved harmonic pulse trains obtained from the spectra presented in Fig. 3(b1). The local frequency spacing of the harmonics $\delta\omega$ determines the interval $T = 2\pi/\delta\omega$ of the attosecond pulse train. Without angular chirp, $\delta\omega = 2\omega_0$ and $T = \pi/\omega_0$, i.e., there are two pulses per cycle of the fundamental. For angularly chirped HHG, the frequencies of the harmonics at a small angle are given by $\sin\theta_x(\omega) \approx \theta_x(\omega) = \gamma_0(\omega - q\omega_0)/q$. Thus, the frequency spacing of the harmonics varies with angle $\delta\omega = 2\theta_x/\gamma_0 + 2\omega_0$ and the variation of the period of the attosecond pulse train will vary in the far field as

$$\Delta T = \pi \Delta\theta/\omega_0^2 \gamma_0. \tag{11}$$

For example, in the results presented in Fig. 3(b2), the variation between the attosecond pulse spacing observed at an angle of 0 mrad (T_1) and that observed at 1.75 mrad (T_2) is $T_1 - T_2 = 61$ as, which is in good agreement with the predicted value from Eq. (11) of $\Delta T = 56$ as. The small deviation is related to that observed between the theoretical model and the results of the numerical simulations in the spectral domain [Fig. 3(b1)].

The angular range covered by the harmonic light depends on the input chirp rate γ_0 and the bandwidth of the harmonics, $\Delta\omega_q$ through $\Delta\theta = \gamma_0 \Delta\omega_q/q$. Therefore, the range of variation of the period that can be obtained across the output beam can be estimated as $\Delta T = 2\Delta\omega_q/\omega_q$. This effect is similar to the variation of the wave-front spacing for the fundamental seen in the focus in the lighthouse effect. Note that in the far field, the spectral bandwidth at a selected observation angle for individual harmonics is reduced by the angular dispersion. Equation (10) gives an expression for the local bandwidth that applies equally for the fundamental and the harmonic. Given the scaling of the parameters k_q, w_q, and γ_q, $\tau_q \approx \sqrt{p}\tau_0$, where the τ's refer to the local pulse duration in the far field. Since the local bandwidth of the individual harmonics in the far field is reduced by the angular dispersion, the pulse train of attosecond pulses is correspondingly longer than would be obtained with conventional focusing. However, just as with SSTF pulses in the fundamental, the short pulse duration limited by the angle-integrated spectrum can be recovered by refocusing the harmonic light.

D. Carrier-envelope-phase effects

When working with few-cycle pulses, the carrier-envelope phase (CEP), which is the offset between the envelope and the carrier waves, becomes relevant in the definition of the field amplitude oscillations within the pulse, especially for HHG, which is a highly nonlinear, field-driven process. Therefore, when working with few-cycle laser pulses, a well-defined and stabilized CEP is required [13,35]. In Fig. 4 we analyze the variation of the angularly chirped HHG with the CEP of the driving field. In Figs. 4(a) and 4(b) we present the electric field at focus at three different transversal positions for $\phi_{CEO} = 0$ and $\phi_{CEO} = \pi/2$. We observe that along the transversal direction, the driving field changes its CEP, covering all possible CEP values. Since the wave fronts are parallel to each other, the variation of the CEP with x follows the pulse front tilt,

$$\phi_{CEO}(x) = \omega_0 \tau_g(x) = \gamma_0 \frac{\omega_0^2}{c} x. \tag{12}$$

As a consequence, we expect that the far-field harmonic distribution should not depend on the CEP of the driving field. In Fig. 4(c) we show the HHG spectrum (linear scale) detected at two angles (0 mrad, solid lines; 1.7 mrad, dashed lines) for $\phi_{CEO} = 0$ (green) and $\phi_{CEO} = \pi/2$ (pink). We observe that apart from a small difference in the yield, there is indeed, as expected, no CEP dependence of the angularly chirped spectrum.

IV. SUMMARY

In summary, we have proposed a technique to enhance the control over the spectral and temporal scales in high-order-harmonic generation by using laser pulses with angular spatial chirp. In contrast to the lighthouse effect, which exploits a transverse chirp at the focal plane to separate attosecond pulses, we have analyzed the use of a pulse with angular spatial chirp at the focal plane where the wave fronts are parallel to each other. According to the results of our numerical simulations, this technique, which does not depend on the CEP of the driver pulse, contributes to improve the spectral and temporal resolution in ultrafast absorption experiments. The single-atom conversion efficiency is expected to be independent of the angular chirp, and the overall conversion efficiency should be comparable to experiments with conventional focusing into a gas jet target. We anticipate that full grating-free hyperspectral dispersion could be achieved by combining simultaneous spatiotemporal focusing HHG with the recently demonstrated noncollinear mixing of counter-rotating polarization pulses [36], which has been shown to separate harmonics in the far field.

[1] P. Agostini and L. F. DiMauro, Rep. Progr. Phys. **67**, 813 (2004).

[2] P. B. Corkum and F. Krausz, Nat. Phys. **3**, 381 (2007).

[3] M. B. Gaarde, J. L. Tate, and K. J. Schafer, J. Phys. B **41**, 132001 (2008).

[4] F. Krausz and M. Ivanov, Rev. Mod. Phys. **81**, 163 (2009).

[5] T. Popmintchev, M. C. Chen, P. Arpin, M. M. Murnane, and H. C. Kapteyn, Nat. Photon. **4**, 822 (2010).

[6] M. Chini, K. Zhao, and Z. Chang, Nat. Photon. **8**, 178 (2014).

[7] J. Miao, T. Ishikawa, I. K. Robinson, and M. M. Murnane, Science **348**, 530 (2015).

[8] K. J. Schafer, B. Yang, L. F. DiMauro, and K. C. Kulander, Phys. Rev. Lett. **70**, 1599 (1993).

[9] P. B. Corkum, Phys. Rev. Lett. **71**, 1994 (1993).

[10] T. Popmintchev, M. Chen, D. Popmintchev, P. Arpin, S. Brown, S. Ališauskas, G. Andriukaitis, T. Balčiunas, O. Mücke, A. Pugzlys, A. Baltuška, B. Shim, S. E. Schrauth, A. Gaeta, C. Hernández-García, L. Plaja, A. Becker, A. Jaroń-Becker, M. M. Murnane, and H. C. Kapteyn, Science **336**, 1287 (2012).

[11] I. P. Christov, M. M. Murnane, and H. C. Kapteyn, Phys. Rev. Lett. **78**, 1251 (1997).

[12] P. M. Paul, E. S. Toma, P. Breger, G. Mullot, F. Augé, Ph. Balcou, H. G. Muller, and P. Agostini, Science **292**, 1689 (2001).

[13] R. Kienberger, E. Goulielmakis, M. Uiberacker, A. Baltuška, V. Yakovlev, F. Bammer, A. Scrinzi, Th. Westerwalbesloh, U. Kleineberg, U. Heinzmann, M. Drescher, and F. Krausz, Nature (London) **427**, 817 (2004).

[14] C. Hernández-García, J. A. Pérez-Hernández, T. Popmintchev, M. M. Murnane, H. C. Kapteyn, A. Jaron-Becker, A. Becker, and L. Plaja, Phys. Rev. Lett. **111**, 033002 (2013).

[15] F. Krausz and M. I. Stockman, Nat. Photon. **8**, 205 (2014).

[16] C. Hernández-García, A. Picón, J. San Román, and L. Plaja, Phys. Rev. Lett. **111**, 083602 (2013).

[17] A. Fleischer, O. Kfir, T. Diskin, P. Sidorenko, and O. Cohen, Nat. Photon. **8**, 543 (2014).

[18] H. Vincenti and F. Quere, Phys. Rev. Lett. **108**, 113904 (2012).

[19] J. A. Wheeler, A. Borot, S. Monchoce, H. Vincenti, A. Ricci, A. Malvache, R. Lopez-Martens, and F. Quéré, Nat. Photon. **6**, 829 (2012).

[20] K. T. Kim, C. Zhang, T. Ruchon, J.-F. Hergott, T. Auguste, D. M. Villeneuve, P. B. Corkum, and F. Quéré, Nat. Photon. **7**, 651 (2013).

[21] G. Zhu, J. van Howe, M. Durst, W. Zipfel, and C. Xu, Opt. Express **13**, 2153 (2005).

[22] C. G. Durfee, M. Greco, E. Block, D. Vitek, and J. A. Squier, Opt. Express **20**, 14244 (2012).

[23] D. N. Vitek, D. E. Adams, A. Johnson, P. S. Tsai, S. Backus, C. G. Durfee, D. Kleinfeld, and J. A. Squier, Opt. Express **18**, 18086 (2010).

[24] D. N. Vitek, E. Block, Y. Bellouard, D. E. Adams, S. Backus, D. Kleinfeld, C. G. Durfee, and J. A. Squier, Opt. Express **18**, 24673 (2010).

[25] C. Durfee and J. Squier, IEEE Photon. J. **7**, 1 (2015).

[26] H. Wang, M. Chini, S. Chen, C.-H. Zhang, F. He, Y. Cheng, Y. Wu, U. Thumm, and Z. Chang, Phys. Rev. Lett. **105**, 143002 (2010).

[27] C. Ott, A. Kaldun, P. Raith, K. Meyer, M. Laux, J. Evers, C. H. Keitel, C. H. Greene, and T. Pfeifer, Science **340**, 716 (2012).

[28] D. Oron, E. Tal, and Y. Silberberg, Opt. Express **13**, 1468 (2005).

[29] A. Meier, M. Iliev, J. Squier, and C. Durfee, Opt. Lett. **40**, 4066 (2015).

[30] C. Hernández-García, J. A. Pérez-Hernández, J. Ramos, E. C. Jarque, L. Roso, and L. Plaja, Phys. Rev. A **82**, 033432 (2010).

[31] J. A. Pérez-Hernández, L. Roso, and L. Plaja, Opt. Express **17**, 9891 (2009).

[32] C. Hernández-García, T. Popmintchev, H. Kapteyn, M. Murnane, A. Becker, and A. Jaron-Becker (unpublished).

[33] A. L'Huillier, P. Balcou, S. Candel, K. J. Schafer, and K. C. Kulander, Phys. Rev. A **46**, 2778 (1992).

[34] R. P. Madden, D. L. Ederer, and K. Codling, Phys. Rev. **177**, 136 (1969).

[35] A. Baltuska, T. Udem, M. Uiberacker, M. Hentschel, E. Goulielmakis, C. Gohle, R. Holzwarth, V. S. Yakovlev, A. Scrinzi, T. W. Hänsch, and F. Krausz, Nature (London) **421**, 611 (2003).

[36] D. Hickstein, F. Dollar, P. Grychtol, J. Ellis, R. Knut, C. Hernández-García, D. Zusin, C. Gentry, J. M. Shaw, T. Fan, K. Dorney, A. Becker, A. Jaron-Becker, M. M. Murnane, H. C. Kapteyn, and C. G. Durfee, Nat. Photon. **9**, 743 (2015).